ACS APPLIED MATERIALS & INTERFACES

www.acsami.org

Research Article

Defect-Rich Dopant-Free ZrO_2 Nanoclusters and Their Size-Dependent Ferromagnetism

Xiaoyi Guan, Saurabh Srivastava, Joseph Palathinkal Thomas, Nina F. Heinig, Jung-Soo Kang, Md Anisur Rahman, and Kam Tong Leung*

Cite This: *ACS Appl. Mater. Interfaces* 2020, 12, 48998–49005

Read Online

ACCESS | Metrics & More | Article Recommendations | Supporting Information

ABSTRACT: As an intermediate form of matter between a single atom or molecule and the bulk, nanoclusters (NCs) provide novel properties because of their high surface area-to-volume ratios and distinct physical and electronic structures. These ultrasmall NCs offer a new approach to advance charge−spin manipulation for novel devices, including spintronics and magnetic tunneling junctions. Here, we deposit monosized ZrO_2 NCs over a large area by using gas-phase aggregation followed by *in situ* size selection by a quadrupole mass filter. These size-specific NCs exhibit sub-oxide photoemission features at binding energies that are dependent on the cluster size (from 3 to 9 nm), which are attributed to different oxygen vacancy defect states. These dopant-free ZrO_2 NCs also show strongly size-dependent ferromagnetism, which provides distinct advantages in solubility and homogeneity of magnetism when compared to traditional dilute magnetic semiconductors. A defect-band hybridization-induced magnetic polaron model is proposed to explain the origin of this size-dependent ferromagnetism. This work demonstrates a new protocol of magnetization manipulation by size control and promises potential applications based on these defect-rich size-selected NCs.

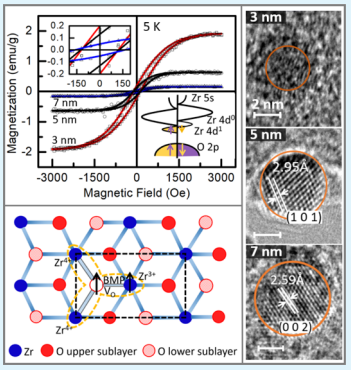

KEYWORDS: *ZrO_2 nanoclusters, gas-phase aggregation, dopant-free ferromagnetic semiconductors, size-dependent ferromagnetism*

INTRODUCTION

Nanoclusters (NCs) are defined as small aggregations of atoms or molecules generally less than 10 nm in size,[1−3] and they are considered to be the link between free atoms or molecules and the bulk. In this interesting size regime, individual states in the electronic structure have not fully merged into bands and remain intact as multiple distinct states. NCs can also be regarded as giant molecules, and they hold the key to understanding the evolution of electronic structures and other properties from single atoms or molecules to the bulk phase with increasing size of the NCs. Because of a significantly higher surface area-to-volume ratio (or specific surface area) compared to their bulk phase, NCs have also attracted a lot of attention in surface-driven research.[11] The high air stability of noble metals such as Au, Ag, and Pt makes their NCs especially attractive to such applications as catalysis,[2] fuel cells,[4] and biosensing.[5,6] The study of transition-metal/metal oxide NCs has also become popular in the past two decades. In addition to the different band structures from the bulk phase, these NCs exhibit notable defects in various oxidation states, which could become dominant and lead to mid-gap states.[2,13,20] These semiconducting oxide NCs with mid-gap states and structures consisting of different ordered arrays and assemblies are strong candidates for applications in light illumination[7] and magnetic sensors.[8] Just as important is the band gap manipulation in Si for microelectronics and in GaAs for photonics, the understanding and control of defects with size-specific NCs over a wide size range are essential to achieve viable applications based on these novel monosized semiconducting oxide NCs.[10]

To date, there are a number of methods to synthesize transition-metal NCs, which include hydrothermal method,[9] self-assembly,[7] and gas-phase aggregation.[2,13,15] With a better understanding and continued advancement of the cluster beam technique,[14] gas-phase aggregation along with size-selective mass filtering technique has become one of the most promising methods to synthesize NCs. Based on a well-developed magnetron sputtering system with an adjustable condensation zone, this technique enables fine-tuning of the cluster size with highly reproducible results. By coupling with a quadrupole mass filter, the system can produce a broad monosized NC beam over a large deposition area.[2,13,16,17] As multiple targets can be placed into the magnetron sputtering system to generate plasma from these targets simultaneously or combinatorically, it is also possible to synthesize a variety of alloy NCs for a wide range of research and technological applications.[18]

Received: August 19, 2020
Accepted: September 29, 2020
Published: October 16, 2020

https://dx.doi.org/10.1021/acsami.0c14706
ACS Appl. Mater. Interfaces 2020, 12, 48998–49005

Recently, ZrO_2 has become an attractive material alternative to TiO_2 for applications such as photoelectrochemical water splitting[21] and fuel cells.[9] Bulk ZrO_2 does not have any magnetic states, whereas an undoped ZrO_2 film obtained by pulsed electron beam deposition in a partial oxygen environment has been found to have a tetragonal structure, showing ferromagnetic properties at room temperature.[22] Similarly, other undoped transition-metal oxides (TiO_2[23] and HfO_2[24]) with surprising ferromagnetic properties have also been reported. Recently, we showed that dopant-free, defect-rich ZrO_2 nanowire and nanobrick films exhibit strong ferromagnetic properties at room temperature.[12] Unlike the conventional dilute magnetic semiconductors (DMSs) such as Mn-doped GaAs or InAs, these undoped ferromagnetic transition-metal oxide nanostructured films have a significantly higher Curie temperature (T_C) than those of conventional DMSs with T_C < 200 K.[27] For materials with promising magnetic applications at room temperature, their Curie temperature should be greater than 500 K.[28] Although some transparent oxide DMSs, such as Cr-doped In_2O_3 films[29] and Co-doped TiO_2 film,[31] have generally high T_C and could therefore serve as a viable material alternative for room-temperature spin-based electronic applications, the solubility of the dopants remains one of the biggest challenges that limit their potential application. Furthermore, the nonuniform distribution of the dopants caused by their natural tendency to form aggregates leads to inhomogeneous magnetism within the material.[32,33] As defects in crystalline structures appear to play an important role in dopant-free ferromagnetic oxides,[12,22] these oxides could have the advantage of uniform magnetization. With the origin of these ferromagnetic properties remaining under debate, the study of defects and the important role that they play in these oxides is therefore fundamentally important to the development of future magnetic devices and spin-based electronics.

Here, we produce size-specific ZrO_2 NCs over the 2−16 nm size regime. Size-tuning is achieved in the gas-phase aggregation technique by using a magnetron sputtering source coupled to a quadrupole mass filter, and the NCs so produced can be deposited uniformly over a large area (2 in. dia.). The as-deposited monosized ZrO_2 NCs (3, 5, 7, and 9 nm in diameter) are oxygen-deficient, and these oxygen-vacancy defects introduce strongly size-dependent ferromagnetic hysteresis. To account for the origin of this ferromagnetism, we propose an improved magnetic polaron generation model involving defect-band hybridization. In addition to this size-dependent ferromagnetism, the high dielectric constant of ZrO_2 also attracts a lot of interest for use as a gate oxide in high electron mobility transistors.[30,35] Biocompatibility and excellent surface charge properties further make ZrO_2 NCs a strong material candidate for nanobiosensors.[36]

MATERIALS AND METHODS

ZrO_2 NCs are directly deposited on hydrogen-terminated Si(100) substrates by using a magnetron-sputterer-based NC generation system (Nanogen 50, Mantis Deposition Ltd.).[2,13] The silicon substrates are cleaned by high-performance liquid chromatography-grade acetone and isopropyl alcohol, each with 10 min of ultrasonication, followed by 5 min of etching in hydrofluoric acid (2 vol %) to remove the native oxide layer, thoroughly rinsed in filtered ultrapure high-resistivity water after each step, and finally dried under a nitrogen stream. The resulting H-terminated Si (H−Si) substrates are then transferred to a high vacuum chamber with a base pressure of 1.5×10^{-8} mbar. The Nanogen source is equipped with three 1 in. dia. DC magnetron sputtering heads, the power output of which can be individually controlled. The zirconium targets (99.9% purity, ACI Alloys) are sputtered by Ar plasma. The sputtered atoms enter a condensation zone (equipped with a cooling jacket), where the atoms collide with one another and aggregate into clusters.[25] The NCs can be transported by diffusion or carried forward by the Ar buffer gas.[14] As the broad beam containing NCs with a large size distribution is collimated through the condensation aperture, it undergoes mass selection in the quadrupole mass filter region. An appropriate set of AC and DC voltages is applied to the quadrupole mass filter to allow the passage of NCs with the preselected mass-to-charge ratio. The size selection process produces a monosized NC beam up to 10^6 amu with a 2% deviation.[13] As no bias is applied on the substrate, the clusters are deposited on the substrate under soft-landing condition. In the present work, we focus on clusters smaller than 10 nm and investigate the nanosize dependency of their magnetic properties.

The surface morphology of the deposited NC film is characterized by field emission scanning electron microscopy (SEM) with a Zeiss Merlin microscope and by atomic force microscopy (AFM) using a Digital Instruments Dimension 3100 Nanoman Nanoscope operating in tapping mode. The crystalline structure of individual clusters is determined by transmission electron microscopy (TEM) with a Zeiss Libra 200 MC microscope with a double-corrected Omega filter operated at 200 kV. The TEM specimen is prepared by depositing the clusters directly on a 300 mesh copper grid with a lacey carbon film using the Nanogen source. The crystal structure of the NC film deposited on a Si substrate is measured by glancing-incidence X-ray diffraction in a PANalytical MRD X'pert Pro diffractometer equipped with a Cu Kα source and a parallel X-ray beam setup operated at an incident angle of $\omega = 0.3°$ over the selected 2θ range. The chemical-state composition of the NC film is characterized by X-ray photoelectron spectroscopy (XPS) using a Thermo-VG Scientific ESCALab 250 microprobe with a monochromatic Al Kα X-ray source (1486.6 eV). The XPS features are fitted by using the CasaXPS software after appropriately removing the Shirley background. To characterize the magnetic properties at different temperatures, the ZrO_2 NCs are deposited onto a 5×5 mm^2 Si substrate to allow the sample to be mounted on a quartz sample holder for superconducting quantum interference device (SQUID) magnetometry in a Quantum Design MPMS SQUID-VSM. After appropriately removing the diamagnetic contribution from the Si substrate and the sample holder to the signal, the magnetization of the ZrO_2 NC film is normalized by mass, as converted by volume estimation using AFM data (without considering the filling factor, shown in Figure S4) and a bulk density of 5.68 g/cm^3. Care is taken to prevent magnetic cross-contamination by using only plastic tweezers and quartz sample holders in all our sample preparation and data collection processes.

RESULTS AND DISCUSSION

The formation and growth of ZrO_2 NCs, obtained by using a magnetron sputterer-based source and a condensation chamber, involve the following mechanism:

$$\mathrm{M + M + Ar + Ar^+ + e^-} \rightarrow \mathrm{M_2^- + Ar^+ + Ar\ (seed\ formation)}$$

$$\mathrm{M_m^- + M \rightarrow M_{m+1}^-\ (aggregation)}$$

$$\mathrm{M_m^- + substrate \rightarrow M_m(ad) + substrate + e^-\ (landing\ and\ neutralization)}$$

$$\mathrm{M_m(ad) + substrate + O_2 \rightarrow M_mO_x(ad) + substrate\ (oxidation)}$$

where Ar is the buffer gas, M_m (m = 2, 3,..., n) is a free metal cluster species, M_m(ad) is a metal cluster adspecies on the

https://dx.doi.org/10.1021/acsami.0c14706
ACS Appl. Mater. Interfaces 2020, 12, 48998−49005

substrate, and M_mO_x(ad) is an oxidized cluster adspecies on the substrate. As the free Zr atoms start to form nucleation seeds upon collision with one another and with the buffer gas within a restricted region from the sputter target, the seeds grow into bigger and bigger clusters as more free atoms become attached to the seed surface.[17] Both the aggregation length (AL), defined as the separation between the top of the sputter target and the exit aperture (Figure 1a), and the Ar gas

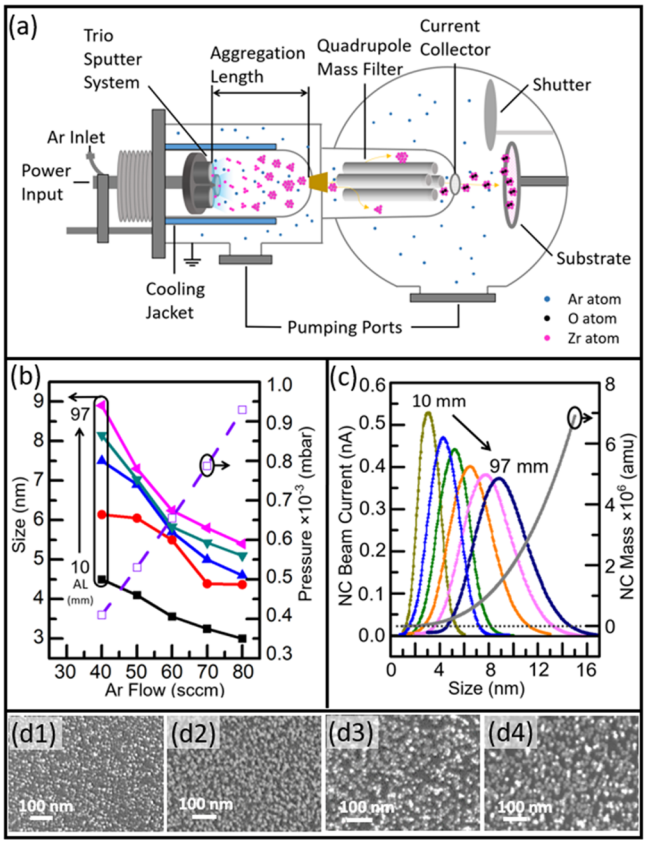

Figure 1. (a) Schematic representation of the Nanogen NC deposition system for producing a size-selected NC beam, which involves (i) generation of free atoms by DC magnetron sputtering, (ii) seed formation by collision and atom aggregation into bigger clusters, and (iii) beam collimation via a 3 mm diameter entrance aperture and size selection of the NCs by a quadrupole mass filter. (b) Mode cluster size (in diameter, left axis) and the deposition chamber pressure (right axis) as a function of Ar flow rate (from 40 to 80 sccm in steps of 10 sccm) for different ALs (10, 30, 50, 70, and 97 mm). The mode cluster size corresponds to the size (diameter) of the maximum in the cluster size distribution. (c) Cluster size distribution, as reflected by the beam current obtained at the collector of the quadrupole mass filter, for a fixed Ar flow rate (50 sccm) and different ALs (10, 30, 50, 70, 90, and 97 mm), along with the mass of Zr NCs (right axis) for different NC sizes. SEM images of ZrO_2 NCs with selected sizes of (d1) 3, (d2) 5, (d3) 7, and (d4) 9 nm as-deposited on H−Si substrates for 60 min by using appropriately optimized deposition parameters and quadrupole mass filter operating voltages.

flow could critically affect this cluster formation process. Figure 1b shows that increasing the Ar flow at a fixed AL promotes the growth of clusters with a smaller size. The buffer gas is therefore not only important for generating plasma to sputter the Zr target and for carrying the clusters forward to the deposition chamber and onto the substrate but also crucial for facilitating the seed formation that leads to the cluster beam becoming negatively charged.[2,25] A higher Ar flow rate promotes the formation of a larger amount of seeds and causes a smaller dwell time for the seeds to pass through the aggregation chamber and therefore reduces the extent of the NC growth for a fixed AL, both of which effectively reduce the overall size of the NCs. On the other hand, increasing the AL for a selected Ar flow would increase the dwell time of the NCs passing through the chamber, therefore promoting a larger mode cluster size and a broader near-Gaussian size distribution (Figure 1c). Figure 1b also shows that increasing the Ar flow from 40 to 80 sccm reduces the cluster diameter at a greater rate for a larger AL than a smaller AL. As a smaller AL has already limited the dwell time for nucleation, the effect of the Ar flow becomes less prominent. In contrast, the Ar flow for a larger AL appears more effective in changing the dwell time. By optimizing both the Ar flow and the AL, the desired size of the NCs can be tuned from 2 to 10 nm (in diameter), and the smallest NC (of 3 nm in mode size) is obtained for an AL of 10 mm at an Ar flow of 80 sccm. By either passing O_2 into the deposition chamber or exposure to the ambient air atmosphere, the Zr NCs could be easily oxidized during the deposition process or upon removal from the chamber.[19] Further details of tuning the dimensions of the clusters with various parameters are discussed elsewhere.[2,13,16−19,25]

Figure 1d1−d4 shows the SEM images of the surface morphology of size-selected ZrO_2 NC films. The NCs are directly deposited on H−Si substrates for 60 min with appropriately optimized deposition parameters (AL and Ar flow) and with the quadrupole set to filter the selected mass (i.e., the peak position of each size distribution curve). Evidently, the as-deposited NCs are dispersed on the substrate into groups or islands of clusters, and these islands of clusters are spread over the substrate producing a NC film with increasing deposition time. The NCs are found to have a near-spherical shape, and they also appear very similar to one another in size, which confirms that the quadrupole mass filter provides good size selection with a narrow size distribution.

Figure 2 shows the low-magnification TEM images of groups of ZrO_2 NCs (with different mode sizes as set by the Nanogen). The center insets depict the narrow size distributions of the NCs produced by the Nanogen, thus demonstrating its excellent size selection. The near-spherical shape of the NCs also indicates that there is no discernible deformation of the ZrO_2 NCs deposited under the soft-landing condition.[2,13] From the high-resolution phase contrast TEM images (Figure 2, top right insets), the ZrO_2 NCs show well-defined crystallinity for the NC size of 5 nm or above. The interplanar spacings of the 5 nm (and 9 nm) and 7 nm NCs are found to be 2.95 and 2.59 Å, respectively, which are in good accord with those of the (1 0 1) and (0 0 2) planes of the tetragonal ZrO_2 lattice. The degree of crystallinity of the tetragonal ZrO_2 NC film is also confirmed by our XRD profiles (Figure S1). On the other hand, the 3 nm NCs appear to be amorphous, likely due to the short dwell time available for the crystalline growth. This is also supported by the corresponding fast Fourier transform (FFT) patterns of the TEM images of individual NCs (Figure 2, bottom right insets), which show a notable contrast between the spot pattern of the crystalline 5 nm NC (Figure 2b) and the ring pattern of the amorphous 3 nm NC (Figure 2a). These amorphous NCs with ultrasmall size could contain a higher density of defects that would likely give rise to stronger magnetic properties.[2,13] It is of interest to note that for bulk ZrO_2 the most stable phase is the monoclinic

https://dx.doi.org/10.1021/acsami.0c14706
ACS Appl. Mater. Interfaces 2020, 12, 48998−49005

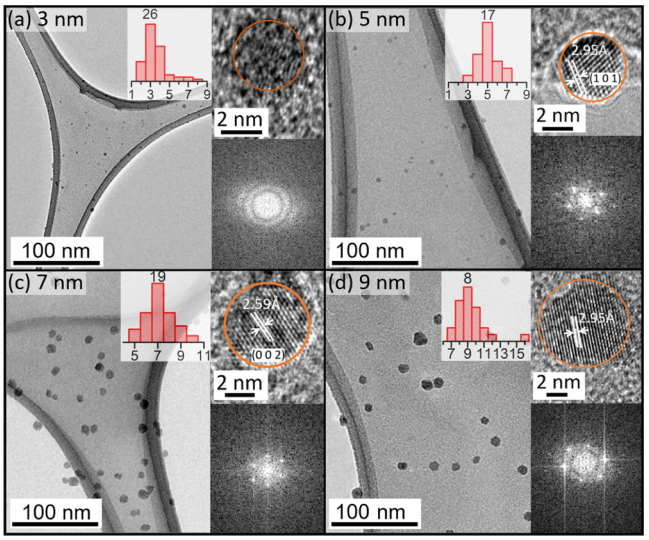

Figure 2. TEM images of a group of ZrO_2 NCs deposited on a TEM copper grid with a lacey carbon film obtained at low magnification with mode sizes of (a) 3, (b) 5, (c) 7, and (d) 9 nm, along with the individual NC of each size obtained at high resolution (top right insets) and the corresponding simulated diffraction patterns generated by FFT (bottom right insets). The NCs so obtained exhibit a very narrow size distribution, as shown in the respective center insets (where the bar label shows the number of NCs with the corresponding mode size in the TEM image), as selected by the quadrupole mass filter in the Nanogen source.

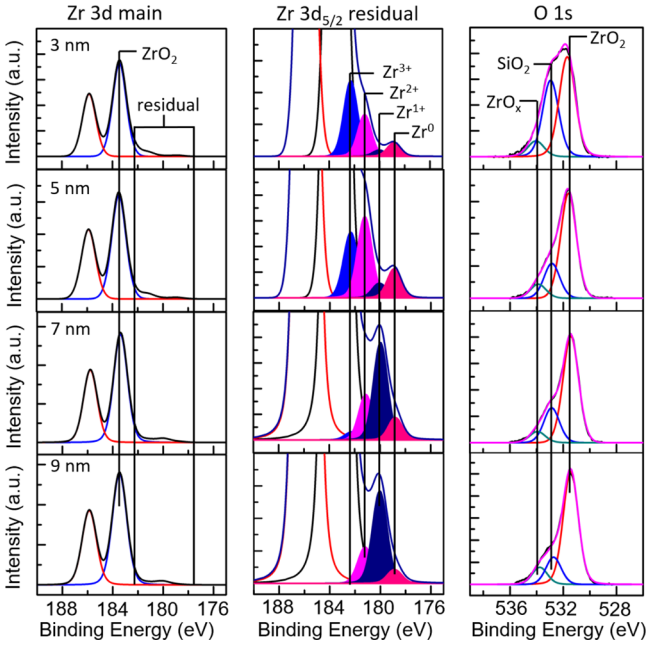

Figure 3. XPS spectra of the Zr 3d region (left column), along with the expanded view of the fitted residual intensities of the Zr $3d_{5/2}$ region (middle column), and the O 1s region (right column) of ZrO_2 NCs of different sizes (3, 5, 7, and 9 nm) as-deposited on H−Si substrates.

Table 1. Comparison of ZrO_x Chemical-State Content, Saturated Magnetization (M_s), Remanence (M_r), and Coercivity (H_c) Measured at 5 and 300 K for ZrO_2 NC Films of Different NC Sizes

NC size (dia.)		3 nm	5 nm	7 nm	9 nm
number of Zr atoms		606	2809	7696	16,383
mass ($\times 10^3$ amu)		55.3	256	702	1490
surface-to-volume ratio (nm^{-1})		2.00	1.20	0.86	0.67
NC film thickness (nm)		4.9	6.1	35.2	34.6
sample volume ($\times 10^{-7}$ cm^3)		1.20	1.49	8.62	8.48
sample mass (μg)		0.68	0.85	4.90	4.82
relative residual intensity in Zr 3d content		10.6%	8.6%	5.7%	4.5%
5 K	M_s (emu/g)	1.91	0.54	0.16	NA
	M_r (emu/g)	0.20	0.11	0.05	NA
	H_c (Oe)	120	125	162	NA
300 K	M_s (emu/g)	1.80	0.46	0.13	NA
	M_r (emu/g)	0.12	0.07	0.02	NA
	H_c (Oe)	77	79	94	NA

phase, followed by the tetragonal and cubic phases. Because of the difference in the surface free energy of the nanostructure within the sub-10 nm size regime, the tetragonal ZrO_2 NCs can be formed and become stable at room temperature.[22,38]

Figure 3 shows the XPS spectra of the Zr 3d and O 1s regions of the as-deposited ZrO_2 NC films. The survey spectra (Figure S2) indicate the presence of Zr, O, C, and Si. It should be noted that the presence of a minute amount of carbon in the form of a carbonaceous layer is often found on samples due to normal handling in air. Evidently, there are no features corresponding to Mn 2p at 638.3 eV, Fe 2p at 706.8 eV, Co 2p at 779.4 eV, and Ni 2p at 852.6 eV, which confirms that the ferromagnetic signals are generated by the ZrO_2 NCs and not any magnetic impurities. The predominant Zr $3d_{5/2}$ feature at 183.4 eV and the prominent O 1s feature at 531 eV (Figure 3) correspond to the Zr^{4+} cation in stoichiometric ZrO_2. The residual intensities between the Zr^{4+} and metallic Zr^0 peaks can be attributed to oxygen-deficient ZrO_x (Table 1). Evidently, the residual band corresponding to ZrO_x shifts from 181 eV to the binding energy position of metallic Zr (at 178.9 eV) with decreasing intensity as the NC size increases from 5 to 9 nm. Based on the binding energies of Zr^{1+} (179.8 eV), Zr^{2+} (180.9 eV), and Zr^{3+} (182.1 eV), we attribute the ZrO_x band to a combination of these oxidation states, which are used in the fitting (Figure 3).[26] More details of the composition of the residual features are given in Table S1 (Supporting Information). For the 3 and 5 nm NCs, the ZrO_x features consist largely of Zr^{3+} and Zr^{2+} contributions. For the larger 7 and 9 nm NCs, the respective Zr^{3+} residual intensities have become extremely low, and the predominant contributions are Zr^{2+} and Zr^{1+}. For the O 1s spectra, after removing the SiO_2 feature at 532.9 eV, the remaining feature at 533.5 eV can be attributed to oxygen-deficient ZrO_x. As the deposition is performed in a low vacuum condition, the aggregated Zr NCs are oxidized in ambient conditions, which could produce nonstoichiometric oxide states.[2] While the surface-to-volume ratio increases with decreasing NC size from 9 to 3 nm for an individual NC, the total specific surface area increases with decreasing NC size. As the formation of ZrO_x could be caused by the presence of oxygen vacancies at locations with low coordination (i.e., in the near-surface region) in the NCs, the smaller NCs are more favorable to introduce oxygen vacancies. As the surface of the NC becomes oxidized with various states, more discernible ferromagnetic properties are expected if the surface is populated with oxygen-deficient sites.

As the substrate has significantly greater mass than the deposited NCs, the main contribution to the sample (NCs +

https://dx.doi.org/10.1021/acsami.0c14706
ACS Appl. Mater. Interfaces 2020, 12, 48998−49005

substrate) during the SQUID magnetometer measurement is expected to be dominated by the silicon substrate. After subtracting the diamagnetic signals from the silicon substrate and quartz sample holder (Figure S3a), we observe a hysteresis loop in the respective magnetization curves of the NC films. In order to perform quantitative analysis of the loop, we minimize the effect of noise by employing a curve-fitting procedure developed by von Dobeneck.[34,37] This procedure is based on the symmetry of the loop and the use of hyperbolic functions, the details of which are provided in the Supporting Information (Figure S3). The magnetization is normalized by the mass of the NC film, which is estimated from the volume of the NC film (Table 1) obtained from the NC film thickness measurements (Figure S4).

Figure 4a,b shows magnetization as a function of magnetic field (the $M-H$ curves) of the monosized ZrO_2 NC films, with

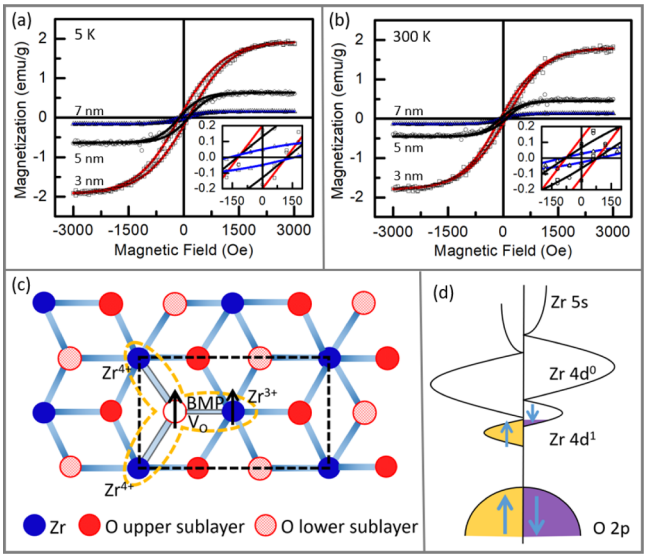

Figure 4. Measured (symbols) and fitted ferromagnetic hysteresis loops (solid lines) of as-grown ZrO_2 NCs of different sizes obtained at (a) 5 and (b) 300 K. (c) Schematic presentation of the formation of magnetic polarons in an unreconstructed ZrO_2 (1 0 1) surface. The missing oxygen vacancy (V_O) in the lower sublayer triggers four nearby Zr ions (the one below V_O is not shown) with two excess electrons. The electron trapping in the oxygen vacancy could couple with the other electron located in Zr^{3+} via exchange interaction, generating the magnetic polaron. (d) Schematic diagram of band-splitting leading to ferromagnetism generation: an impurity band contributed by Zr $4d^1$ (Zr^{3+}) is generated by the oxygen vacancy defects. This impurity band could merge and hybridize with the conduction band, which triggers band-splitting into spin-up and spin-down states.

the three smallest NC sizes (3, 5, and 7 nm), obtained at 5 K and room temperature. Evidently, all the NC films start to reach saturation at 2000 Oe. Although the magnetization curves measured at room temperature appear noisier than those at 5 K, they clearly follow the characteristic ferromagnetic profile (after the respective contributions from the substrate and the sample holder have been appropriately removed). The magnetic saturation (M_s), remanence (M_r), and coercivity (H_c) are calculated from the corresponding fitted $M-H$ curves and are summarized in Table 1. Among the monosized NCs, the 3 nm ZrO_2 NCs exhibit the strongest M_s and M_r, both at 5 and 300 K. The M_s value for the 5 nm NCs (0.54 emu/g at 5 K) is found to decrease significantly to 28% of that of the 3 nm NCs (1.91 emu/g at 5 K), and M_s continues to decrease as the NC size increases to 7 nm (0.16 emu/g at 5 K). However, the 9 nm NCs start to show bulk-like properties without any ferromagnetism (Figure S3d). The changes in magnetization are likely due to the changes in the defect concentration and in the NC packing density on the substrate. As the NCs are deposited on the substrate under soft-landing condition, they are expected to be loosely packed and stacked on the substrate without deformation. There is therefore more space among the larger NCs, which reduces their material density. On the other hand, H_c is found to increase slightly from the 3 nm ZrO_2 NCs (120 Oe at 5 K) to 5 nm (125 Oe) and to 7 nm NCs (162 Oe). For the 9 nm NCs, the nearly linear and noisy magnetization curve (Figure S3d) suggests that these larger NCs start to essentially follow the bulk (paramagnetic) profile. Except for the smaller corresponding values, the trends in M_s and H_c observed for the magnetization curves measured at 300 K generally follow those at 5 K with respect to the changes in the NC size, which suggests that there is no phase change between 5 and 300 K. Furthermore, it should be noted that we have also performed postannealing of the as-grown ZrO_x NCs in O_2 in order to "heal" (or reduce the amount of) the oxygen vacancy defects. These postannealed samples do not exhibit any ferromagnetism, which confirms that the observed ferromagnetism comes from the oxygen vacancies.

To date, there are only a few theoretical studies on magnetic ordering and the origin of magnetic semiconductor oxides. In the bound magnetic polaron (BMP) model, which is highly applicable to materials with transition-metal dopants, magnetic coupling is generated via exchange interaction between the donors and local magnetic ions, resulting in a cloud of polarized spins and the so-called ferromagnetic alignment.[40] In a dopant-free semiconductor oxide material, the grain boundary defects that are proposed to correspond to oxygen vacancies have strong effects on their interactions. The magnetic exchange interaction is enhanced by a high concentration of the oxygen vacancy defects overlapping among the BMPs. However, this model could not explain how this ferromagnetism could exist at room temperature or in some other nonferromagnetic materials with a high concentration of oxygen vacancies.[12,41] In the charge-transfer ferromagnetism (CTF) model, developed as an extension of the BMP model, the high defect concentration contributes to an impurity band. Electron hopping between the impurity band and the charge reservoir created by the dopants leads to splitting of the spin states.[28,29,39] As the ZrO_2 NCs obtained in the present work do not have any dopant, the observed ferromagnetism for the clusters of different sizes is therefore related to oxygen vacancy defects. The presence of oxygen vacancy defects is in good accord with the XPS residual intensities of the Zr 3d feature between 179 and 182 eV and the O 1s feature between 532 and 536 eV attributed to ZrO_x (Figure 3).

Based on the previous theoretical studies involving the BMP and CTF models and our XPS analysis, we propose a band hybridization model to explain the size-dependent ferromagnetism of the ZrO_2 NCs. Unlike Ti in TiO_2 and Zn in ZnO, the Zr atoms in the ZrO_2 bulk are not easily reduced from Zr^{4+} to a lower oxidation state (i.e., Zr^{3+}, Zr^{2+}, or Zr^{1+}).[20] However, in the presence of a high electric field or a surface, it is possible for Zr^{4+} to be reduced to a lower oxidation state.[26,41] In a

https://dx.doi.org/10.1021/acsami.0c14706
ACS Appl. Mater. Interfaces 2020, 12, 48998−49005

recent density functional theory study,[20,38,41] oxygen vacancies are found to have a lower formation energy in a ZrO_2 NC than the bulk ZrO_2, which makes the ZrO_2 NC more favorable to host oxygen-reducible structures. Because of the presence of these oxygen vacancy defects, the ZrO_2 tetragonal phase could become stabilized at room temperature. The oxygen vacancies are more easily formed in a lower-dimensional structure such as the surface of the clusters. There is therefore a higher relative concentration of oxygen vacancy defects (i.e., ZrO_x) in the NC film with smaller NCs because of their higher surface-to-volume ratio (when compared to a uniform film or powders).[38,41] In the tetragonal ZrO_2 structure, one missing oxygen atom (i.e., an oxygen vacancy defect) could trigger the reduction of one of the nearby Zr^{4+} ions to Zr^{3+}, leaving a resonance structure that contains a singly charged oxygen vacancy and a Zr^{3+} ion. The excess 4d electron in the lattice starts to form a magnetic polaron due to the exchange interaction (Figure 4c). As the Zr^{3+} ions become the charge reservoirs as a result of this defect formation, an impurity band arises between the conduction band and valence band. Hybridization between the impurity band and the conduction band causes band-splitting that leads to spin-up and spin-down states, which favors the ferromagnetic ordering (Figure 4d).[12,41] As the size of NC increases and approaches the bulk, there are more nearby missing oxygen atoms (i.e., >2 atoms/unit cell), and more Zr^{2+}, Zr^{1+}, or even Zr^0 (metallic) states are introduced. Although there is a higher concentration of defects along with more unpaired d-shell electrons, too close overlapping of the electron wave functions (leading to exchange interaction) could induce antiparallel alignment and therefore give rise to antiferromagnetism. In addition, the excess electrons in Zr^{1+} and Zr^0 occupying the orbitals individually may lead to paramagnetic property as well. Hence, when the NC size increases from 3 to 9 nm, the concentration of Zr^{3+} decreases (as revealed by the XPS spectra in Figure 3) and less magnetic polarons are produced, which in turn leads to weaker magnetic saturation. The present model is found to be consistent with the recently reported first-principle calculations on even smaller clusters (<3 nm).[41]

Our ferromagnetic NCs are novel and unique because they represent one of the rare dopant-free DMS materials. Our ZrO_2 NCs only require less than 2000 Oe external field to reach saturation. The sensitivity and saturation (1.8 emu/g) are much higher than most of the magnetic transparent oxide materials, including undoped ZrO_2 film (0.18 emu/g),[42] Mn-doped ZrO_2 thin film (0.02 emu/g),[43] and Cu-doped ZnO nanowire film (0.2 emu/g).[44] In addition to presenting further insights of the ferromagnetic property of these NCs, our magnetic ZrO_2 NCs also promise some potential technological applications. In cancer theragnostics, these ultrasmall NCs combined with designer surface chemistries are highly appealing to diagnostic assays and MRI contrast agents.[8] Furthermore, as the ferromagnetism of ZrO_2 NCs are strongly size-dependent, the magnetization can be manipulated by controlling the size. These magnetic NCs with a high dielectric constant could potentially serve as tunnel junctions in future nanoscale spintronic devices.[45]

CONCLUSIONS

In summary, we have successfully synthesized and deposited dopant-free size-selected ZrO_2 NCs of 3, 5, 7, and 9 nm in size on silicon substrates. These monosized NCs exhibit strong size-dependent ferromagnetism. Together with the nature of the nanostructures, the built-in oxygen vacancy defects near the surface of the NCs are found to be responsible for the magnetic properties. Our XPS study further shows that there is a correlation between the magnetization and Zr^{3+} content of the NCs. The present study establishes a strong link between the proposed mechanism involving defect-induced band hybridization and the observed magnetization properties. This work also demonstrates a novel approach to synthesize dopant-free magnetic semiconductors and to manipulate the magnetization by size control. The simplicity of the technique and the room-temperature deposition promise high reproducibility and a wide substrate choice that are attractive to a broad range of applications, such as tunneling junctions and future spintronics.

ASSOCIATED CONTENT

Supporting Information

The Supporting Information is available free of charge at https://pubs.acs.org/doi/10.1021/acsami.0c14706.

XRD profiles of as-deposited ZrO_2 NCs, XPS survey spectra, details of quantitative analysis of magnetization data, AFM height profiles of the ZrO_2 NCs, and relative compositions of Zr 3d oxidation states (PDF)

AUTHOR INFORMATION

Corresponding Author

Kam Tong Leung − *WATLab and Department of Chemistry, University of Waterloo, Waterloo, Ontario N2L 3G1, Canada;* orcid.org/0000-0002-1879-2806; Email: tong@uwaterloo.ca

Authors

Xiaoyi Guan − *WATLab and Department of Chemistry, University of Waterloo, Waterloo, Ontario N2L 3G1, Canada*

Saurabh Srivastava − *WATLab and Department of Chemistry, University of Waterloo, Waterloo, Ontario N2L 3G1, Canada*

Joseph Palathinkal Thomas − *WATLab and Department of Chemistry, University of Waterloo, Waterloo, Ontario N2L 3G1, Canada;* orcid.org/0000-0001-6455-908X

Nina F. Heinig − *WATLab and Department of Chemistry, University of Waterloo, Waterloo, Ontario N2L 3G1, Canada*

Jung-Soo Kang − *WATLab and Department of Chemistry, University of Waterloo, Waterloo, Ontario N2L 3G1, Canada*

Md Anisur Rahman − *WATLab and Department of Chemistry, University of Waterloo, Waterloo, Ontario N2L 3G1, Canada;* orcid.org/0000-0002-3194-881X

Complete contact information is available at: https://pubs.acs.org/10.1021/acsami.0c14706

Notes

The authors declare no competing financial interest.

ACKNOWLEDGMENTS

This work was supported by the Natural Sciences and Engineering Research Council of Canada.

REFERENCES

(1) Ott, L. S.; Finke, R. G. Nanocluster Formation and Stabilization Fundamental Studies: Investigating "Solvent-Only" Stabilization En Route to Discovering Stabilization by the Traditionally Weakly Coordinating Anion BF_4-Plus High Dielectric Constant Solvents. *Inorg. Chem.* **2006**, *45*, 8382−8393.

(2) Srivastava, S.; Thomas, J. P.; Heinig, N.; Abd-Ellah, M.; Rahman, M. A.; Leung, K. T. Efficient Photoelectrochemical Water Splitting on Ultrasmall Defect-Rich TaO_x Nanoclusters Enhanced by Size-Selected Pt Nanocluster Promoters. *Nanoscale* **2017**, *9*, 14395−14404.
(3) Palmer, R. E.; Pratontep, S.; Boyen, H.-G. Nanostructured Surfaces from Size-Selected Clusters. *Nat. Mater.* **2003**, *2*, 443−448.
(4) Zhang, J.; Sasaki, K.; Sutter, E.; Adzic, R. R. Stabilization of Platinum Oxygen-Reduction Electrocatalysts Using Gold Clusters. *Science* **2007**, *315*, 220−222.
(5) Kalita, S.; Kandimalla, R.; Bhowal, A. C.; Kotoky, J.; Kundu, S. Functionalization of β-Lactam Antibiotic on Lysozyme Capped Gold Nanoclusters Retrogress MRSA and Its Persisters Following Awakening. *Sci. Rep.* **2018**, *8*, 5778.
(6) Gong, L.; Kuai, H.; Ren, S.; Zhao, X.-H.; Huan, S.-Y.; Zhang, X.-B.; Tan, W. Ag Nanocluster-Based Label-Free Catalytic and Molecular Beacons for Amplified Biosensing. *Chem. Commun.* **2015**, *51*, 12095−12098.
(7) Liu, Y.; Yao, D.; Zhang, H. Self-Assembly Driven Aggregation-Induced Emission of Copper Nanoclusters: A Novel Technology for Lighting. *ACS Appl. Mater. Interfaces* **2017**, *10*, 12071−12080.
(8) Vamvakidis, K.; Mourdikoudis, S.; Makridis, A.; Paulidou, E.; Angelakeris, M.; Dendrinou-Samara, C. Magnetic Hyperthermia Efficiency and MRI Contrast Sensitivity of Colloidal Soft/Hard Ferrite Nanoclusters. *J. Colloid Interface Sci.* **2018**, *511*, 101−109.
(9) Kim, D.; Kim, H. S.; Park, S.-M.; Ji, M.-J.; Choi, B.-H.; Kang, M. Physicochemical Properties of Ni-Loaded Yttrium Stabilized Zirconia Nanotubes for Solid Oxide Fuel Cells. *J. Ind. Eng. Chem.* **2014**, *20*, 505−511.
(10) Fert, A. Nobel Lecture: Origin, Development, and Future of Spintronics. *Rev. Mod. Phys.* **2008**, *80*, 1517−1530.
(11) Aiken, J. D.; Finke, R. G. A Review of Modern Transition-Metal Nanoclusters: Their Synthesis, Characterization, and Applications in Catalysis. *J. Mol. Catal. A: Chem.* **1999**, *145*, 1−44.
(12) Rahman, M. A.; Rout, S.; Thomas, J. P.; Mcgillivray, D.; Leung, K. T. Defect-Rich Dopant-Free ZrO_2 Nanostructures with Superior Dilute Ferromagnetic Semiconductor Properties. *J. Am. Chem. Soc.* **2016**, *138*, 11896−11906.
(13) Srivastava, S.; Thomas, J. P.; Rahman, M. A.; Abd-Ellah, M.; Mohapatra, M.; Pradhan, D.; Heinig, N. F.; Leung, K. T. Size-Selected TiO_2 Nanocluster Catalysts for Efficient Photoelectrochemical Water Splitting. *ACS Nano* **2014**, *8*, 11891−11898.
(14) Frank, F.; Schulze, W.; Tesche, B.; Urban, J.; Winter, B. Formation of Metal Clusters and Molecules by Means of the Gas Aggregation Technique and Characterisation of Size Distribution. *Surf. Sci.* **1985**, *156*, 90−99.
(15) Das, B.; Balamurugan, B.; Skomski, R.; Li, X. Z.; Mukherjee, P.; Hadjipanayis, G. C.; Sellmyer, D. J. Structure and Magnetism of Dilute Co(Zr) Nanoclusters. *J. Appl. Phys.* **2013**, *113*, 17B509.
(16) Gracia-Pinilla, M.; Martínez, E.; Vidaurri, G. S.; Pérez-Tijerina, E. Deposition of Size-Selected Cu Nanoparticles by Inert Gas Condensation. *Nanoscale Res. Lett.* **2009**, *5*, 180−188.
(17) Shyjumon, I.; Gopinadhan, M.; Helm, C. A.; Smirnov, B. M.; Hippler, R. Deposition of Titanium/Titanium Oxide Clusters Produced by Magnetron Sputtering. *Thin Solid Films* **2006**, *500*, 41−51.
(18) Ayesh, A. I. Size-Selected Fabrication of Alloy Nanoclusters by Plasma-Gas Condensation. *J. Alloys Compd.* **2018**, *745*, 299−305.
(19) Drabik, M.; Choukourov, A.; Artemenko, A.; Polonskyi, O.; Kylian, O.; Kousal, J.; Nichtova, L.; Cimrova, V.; Slavinska, D.; Biederman, H. Structure and Composition of Titanium Nanocluster Films Prepared by a Gas Aggregation Cluster Source. *J. Phys. Chem. C* **2011**, *115*, 20937−20944.
(20) Puigdollers, A. R.; Illas, F.; Pacchioni, G. Effect of Nanostructuring on the Reactivity of Zirconia: A DFT+*U* Study of Au Atom Adsorption. *J. Phys. Chem. C* **2016**, *120*, 17604−17612.
(21) Rahman, M. A.; Thomas, J. P.; Leung, K. T. A Delaminated Defect-Rich ZrO_2 Hierarchical Nanowire Photocathode for Efficient Photoelectrochemical Hydrogen Evolution. *Adv. Energy Mater.* **2017**, *8*, 1701234.
(22) Ning, S.; Zhan, P.; Xie, Q.; Li, Z.; Zhang, Z. Room-Temperature Ferromagnetism in Un-Doped ZrO2 Thin Films. *J. Phys. D: Appl. Phys.* **2013**, *46*, 445004.
(23) Hong, N. H.; Sakai, J.; Poirot, N.; Brizé, V. Room-Temperature Ferromagnetism Observed in Undoped Semiconducting and Insulating Oxide Thin Films. *Phys. Rev. B: Condens. Matter Mater. Phys.* **2006**, *73*, 132404.
(24) Venkatesan, M.; Fitzgerald, C. B.; Coey, J. M. D. Unexpected Magnetism in a Dielectric Oxide. *Nature* **2004**, *430*, 630.
(25) Khojasteh, M.; Kresin, V. V. Influence of Source Parameters on the Growth of Metal Nanoparticles by Sputter-Gas-Aggregation. *Appl. Nanosci.* **2017**, *7*, 875−883.
(26) Ma, W.; Herbert, F. W.; Senanayake, S. D.; Yildiz, B. Non-Equilibrium Oxidation States of Zirconium during Early Stages of Metal Oxidation. *Appl. Phys. Lett.* **2015**, *106*, 101603.
(27) Dietl, T. Ten-Year Perspective on Dilute Magnetic Semiconductors and Oxides. *Nat. Mater.* **2010**, *9*, 965−974.
(28) Coey, J. M. D.; Venkatesan, M.; Fitzgerald, C. B. Donor Impurity Band Exchange in Dilute Ferromagnetic Oxides. *Nat. Mater.* **2005**, *4*, 173−179.
(29) Philip, J.; Punnoose, A.; Kim, B. I.; Reddy, K. M.; Layne, S.; Holmes, J. O.; Satpati, B.; Leclair, P. R.; Santos, T. S.; Moodera, J. S. Carrier-Controlled Ferromagnetism in Transparent Oxide Semiconductors. *Nat. Mater.* **2006**, *5*, 298−304.
(30) Ryu, S. W.; Cho, S.; Park, J.; Kwac, J.; Kim, H. J.; Nishi, Y. Effects of ZrO_2 Doping on HfO_2 Resistive Switching Memory Characteristics. *Appl. Phys. Lett.* **2014**, *105*, 072102.
(31) Ding, X.; Cui, X.; Xiao, C.; Luo, X.; Bao, N.; Rusydi, A.; Yu, X.; Lu, Z.; Du, Y.; Guan, X.; Tseng, L.-T.; Lee, W. T.; Ahmed, S.; Zheng, R.; Liu, T.; Wu, T.; Ding, J.; Suzuki, K.; Lauter, V.; Vinu, A.; Ringer, S. P.; Yi, J. B. Confinement-Induced Giant Spin−Orbit-Coupled Magnetic Moment of Co Nanoclusters in TiO_2 Films. *ACS Appl. Mater. Interfaces* **2019**, *11*, 43781−43788.
(32) Bonanni, A.; Dietl, T. A Story of High-Temperature Ferromagnetism in Semiconductors. *Chem. Soc. Rev.* **2010**, *39*, 528−539.
(33) Liu, W.; Zhang, H.; Shi, J.-A.; Wang, Z.; Song, C.; Wang, X.; Lu, S.; Zhou, X.; Gu, L.; Louzguine-Luzgin, D. V.; Chen, M.; Yao, K.; Chen, N. A Room-Temperature Magnetic Semiconductor from a Ferromagnetic Metallic Glass. *Nat. Commun.* **2016**, *7*, 13497.
(34) von Dobeneck, T. Systematic Analysis of Natural Magnetic Mineral Assemblages Based on Modelling Hysteresis Loops with Coercivity-Related Hyperbolic Basis Functions. *Geophys. J. Int.* **1996**, *124*, 675−694.
(35) Javey, A.; Kim, H.; Brink, M.; Wang, Q.; Ural, A.; Guo, J.; Mcintyre, P.; Mceuen, P.; Lundstrom, M.; Dai, H. High-κ Dielectrics for Advanced Carbon-Nanotube Transistors and Logic Gates. *Nat. Mater.* **2002**, *1*, 241−246.
(36) Kumar, S.; Sharma, J. G.; Maji, S.; Malhotra, B. D. Nanostructured Zirconia Decorated Reduced Graphene Oxide Based Efficient Biosensing Platform for Non-Invasive Oral Cancer Detection. *Biosens. Bioelectron.* **2016**, *78*, 497−504.
(37) Jackson, M.; Solheid, P. On the Quantitative Analysis and Evaluation of Magnetic Hysteresis Data. *Geochem., Geophys., Geosyst.* **2010**, *11*, Q04Z15.
(38) Puigdollers, A. R.; Illas, F.; Pacchioni, G. ZrO_2 Nanoparticles: A Density Functional Theory Study of Structure, Properties and Reactivity. *Rend. Fis. Acc. Lincei.* **2017**, *28*, 19−27.
(39) Coey, J. M. D.; Wongsaprom, K.; Alaria, J.; Venkatesan, M. Charge-Transfer Ferromagnetism in Oxide Nanoparticles. *J. Phys. D: Appl. Phys.* **2008**, *41*, 134012.
(40) Yakovlev, D. R.; Ossau, W. In *Introduction to the Physics of Diluted Magnetic Semiconductors*; Gaj, J.; Kossut, J., Eds.; Springer: Heidelberg, Berlin, 2010, pp 221−262.
(41) Albanese, E.; Ruiz Puigdollers, A.; Pacchioni, G. Theory of Ferromagnetism in Reduced ZrO_{2-x} Nanoparticles. *ACS Omega* **2018**, *3*, 5301−5307.

https://dx.doi.org/10.1021/acsami.0c14706
ACS Appl. Mater. Interfaces 2020, 12, 48998−49005

(42) Ning, S.; Zhang, Z. Phase-Dependent and Defect-Driven d^0 Ferromagnetism in Undoped ZrO_2 Thin Films. *RSC Adv.* **2015**, *5*, 3636−3641.
(43) Hong, N. H.; Park, C.-K.; Raghavender, A. T.; Ciftja, O.; Bingham, N. S.; Phan, M. H.; Srikanth, H. Room Temperature Ferromagnetism in Monoclinic Mn-Doped ZrO_2 Thin Films. *J. Appl. Phys.* **2012**, *111*, 07C302.
(44) Wan, W.; Huang, J.; Zhu, L.; Hu, L.; Wen, Z.; Sun, L.; Ye, Z. Defects Induced Ferromagnetism in ZnO Nanowire Arrays Doped with Copper. *CrystEngComm* **2013**, *15*, 7887.
(45) Ogale, S. B. Dilute Doping, Defects, and Ferromagnetism in Metal Oxide Systems. *Adv. Mater.* **2010**, *22*, 3125−3155.

https://dx.doi.org/10.1021/acsami.0c14706
ACS Appl. Mater. Interfaces 2020, 12, 48998−49005